Electromagnetic dissociation of relativistic ^{28}Si

J. Barrette,[3] R. Bellwied,[6,a] P. Braun-Munzinger,[6] W.E. Cleland,[5] G. David,[6,b] J. Dee,[6] O. Dietzsch,[7] E. Duek,[1,c] M. Fatyga,[1] D. Fox,[2,d] S.V. Greene,[9,e] J.R. Hall,[4,a] T.K. Hemmick,[9,f] N. Herrmann,[6,g] B. Hong,[6] K. Jayananda,[5,h] D. Kraus,[5] B.S. Kumar,[9] R. Lacasse,[3] D. Lissauer,[1] W.J. Llope,[6,i] T. Ludlam,[1] S.K. Mark,[3] S. McCorkle,[1] J.T. Mitchell,[9,j] M. Muthuswamy,[6,k] E. O'Brien,[1] C. Pruneau,[3,a] F.S. Rotondo,[9] J. Simon-Gillo,[8,l] U. Sonnadara,[5] J. Stachel,[6] E.M. Takagui,[5,m] H. Takai,[1] T.G. Throwe,[1] L. Waters,[6,l] C. Winter,[9] K. Wolf,[8] D. Wolfe,[4] C.L. Woody,[1] N. Xu,[6,l] Y. Zhang,[6] Z. Zhang,[5] and C. Zou[6]

(E814 Collaboration)

[1] *Brookhaven National Laboratory, Upton, New York 11973*
[2] *Los Alamos National Laboratory, Los Alamos, New Mexico 87545*
[3] *McGill University, Montreal, Quebec H3A 2T8, Canada*
[4] *University of New Mexico, Albuquerque, New Mexico 87131*
[5] *University of Pittsburgh, Pittsburgh, Pennsylvania 15260*
[6] *State University of New York, Stony Brook, New York 11794*
[7] *Universidade de São Paulo, São Paulo, Brazil*
[8] *Texas A&M University, College Station, Texas 77843*
[9] *Yale University, New Haven, Connecticut 06520*

(Received 7 July 1994)

We have studied in detail the electromagnetic dissociation of ^{28}Si projectiles at 14.6 GeV/(c nucleon), interacting with Pb, Sn, Cu, and Al targets. Exclusive cross sections were measured for several decay channels, including final states involving the emission of protons, neutrons, and α particles. Excitation energy distributions for the $1n+^{27}$Si and $2p+^{26}$Mg decay channels were reconstructed with a resolution of 2 MeV, using a constrained kinematic fit. The energy distributions obtained for $1n+^{27}$Si are in good agreement with the $\sigma(\gamma,n)$ photoneutron cross sections multiplied by the virtual photon spectrum obtained in the Weizsäcker-Williams approximation. A search for the double photon excitation process, based on the dependence of the cross sections on the target atomic number, was performed.

PACS number(s): 25.70.Mn, 24.30.Cz, 25.75.+r, 27.30.+t

I. INTRODUCTION

The acceleration of heavy ions to relativistic momenta has opened up the possibility to excite the projectile nuclei electromagnetically to energies of tens (even hundreds) of MeV and therefore to study high-lying excitations such as the giant dipole and quadrupole resonances. The excitation mechanism can be quite well described as the absorption of virtual photons produced by the electromagnetic field of one nucleus (target or projectile) by the other nucleus [1]. For example, at a beam energy of $\approx$ 15 GeV/(c nucleon), heavy targets can generate an intense field of virtual photons up to 5 photons/MeV at 20 MeV. For a typical transverse area of 10^4 fm^2 and a pulse duration of about 1 fm/c, this implies equivalent photon densities of approximately 10^{46}/MeV cm^2 s, far

[a] Present address: Dept. of Physics, Wayne State University, Detroit, MI 48202.
[b] Present address: Brookhaven National Laboratory, Building 510A, Upton, NY 11973.
[c] Present address: SSC Laboratory, MS 1070, 2550 Beckleymeade Ave., Dallas, TX 75248.
[d] Present address: Indiana University Cyclotron Facility, 2401, Bloomington, IN 47405.
[e] Present address: Dept. of Physics, Vanderbilt University, Nashville, TN 37235.
[f] Present address: Dept. of Physics, State University of New York, Stony Brook, NY 11794.
[g] Present address: Physikalisches Institut, Universität Heidelberg, D 69 Heidelberg, Germany.
[h] Present address: Dept. of Physics, University of Sri Jayewardenepura, Nugegoda, Sri Lanka.
[i] Present address: Dept. of Physics, Michigan State University, East Lansing, MI 48824.
[j] Present address: Nuclear Science Division, Lawrence Berkeley Laboratory, Berkeley, CA 94720.
[k] Present address: Dept. of Radiation Oncology, Presbyterian Hospital, Pittsburgh, PA 15260.
[l] Present address: Los Alamos National Laboratory, Los Alamos, NM 87545.
[m] Present address: Instituto de Fisica, Universidade de São Paulo, São Paulo, Brazil.

exceeding photon densities available at electron accelerators. The high photon density brings as a consequence a large cross section for the excitation of resonant states and thus the possibility to investigate harmonics of the giant resonances [2].

The use of relativistic heavy ions for the study of electromagnetic dissociation (EMD) offers a number of experimental advantages, particularly in the identification of specific final states. The projectile is incident with energy $A_p m_N \gamma_o$ (in units with $c = 1$), where A_p is the number of nucleons in the projectile, m_N is the nucleon mass, and γ_o is the Lorentz factor, which is approximately 15 at AGS energies. Because the center-of-mass velocities in the decaying system are quite low relative to the projectile velocity, the laboratory energy of a decay product of mass number A is close to $Am_N\gamma_o$. Thus a measure of this energy to a fractional precision $\Delta E/E \sim 1/A$ is adequate to determine A. Since the magnetic deflection in the spectrometer is proportional to $[(A/Z)m_N\gamma_o]^{-1}$, a measurement of the deflection angle yields the value of A/Z for the residual final-state ion. The atomic number can be directly obtained from a measurement of the specific energy loss. Combining these measurements, which are redundant in the case of charged particles, and using conservation of charge and energy permits unambiguous identification of a large number of exclusive decay channels. The E814 apparatus takes advantage of the characteristics of EMD events at relativistic energies to achieve complete identification on an event-by-event basis for final states involving the emission of protons, neutrons, and α particles.

The cross-section results presented here for the exclusive EMD channels confirm our previous measurements [3] and extend them to a larger number of decay channels. For the three decay channels with the highest cross sections ($1p + {}^{27}$Al, $1n + {}^{27}$Si, and $2p + {}^{26}$Mg) we have carried out a more detailed study which includes a complete kinematic reconstruction event by event. This reconstruction permits a measurement of the final-state energy (the sum of the threshold energy for the reaction and the center-of-mass kinetic energies of the final-state particles) of the system, along with their angular distributions. For the $1p+{}^{27}$Al and $1n+{}^{27}$Si decay channels, it is possible to compare our cross sections as a function of energy to photonuclear cross sections [4–6] at energies where the latter exist, up to about 25 MeV. Also, our three reconstructed channels correspond to more than 80% of the total EMD cross section, and thus it is meaningful to compare the sum of our measured cross sections with total photon absorption measurements made with real photons.

Of particular interest is the possible multiple excitation of giant dipole resonances (GDR), which could be excited in relativistic heavy ion collisions through the absorption of two or more virtual photons of energy $E_\gamma \sim E_{\rm GDR}$. The first experimental verification of the existence of double giant dipole resonances (DGDR) was made in a pion double charge exchange reaction [7]. Recently, indications of the population of these states from EMD induced by beams of very heavy ions produced by the GSI-SIS accelerator have been reported [8–10]. Surprisingly, the measured cross sections are larger by a factor of 2 or more than theoretical predictions [11–16]. In contrast to the GSI experiments our investigations focus on excitation of the relatively light nucleus ^{28}Si and we examine the presence of the DGDR in ^{28}Si in two ways: (a) by examining the dependence of the cross section on the atomic number Z_T of the target nucleus for decay channels with reaction Q-value thresholds close to $E_{\rm DGDR} \sim 2E_{\rm GDR}$ and (b) by searching for an enhancement in the reconstructed excitation energy distributions near $E_{\rm DGDR}$. Note that excitation of the DGDR leads to a Z_T^4 component in the cross section, compared to the dominant Z_T^2 for single excitation (see below).

The paper is organized as follows. In Sec. II we describe the apparatus and the trigger used to collect EMD events. The analysis procedure, including event selection and reconstruction is discussed in Sec. III. Section IV contains the results for cross sections and final-state energy distributions. Conclusions are stated in Sec. V.

II. EXPERIMENTAL SETUP

The experimental setup used in this work is shown in Fig. 1. The coordinate system is defined as a right-handed system whose origin is at the target, with the z axis along the incident beam direction and the y axis vertical (upward). The detectors in the experiment consist of a beam telescope, which defines acceptable beam particles, a pair of silicon strip detectors to measure the horizontal coordinate and angle of the incoming beam particles at the target, a set of detectors in the target area to measure the energy and charge multiplicity, two silicon disks upstream and downstream of the target to measure the charge of the beam particles or residual ions, and a forward spectrometer to measure the position, energy, and charge of the final-state particles. The two dipole magnets M1 and M2 provide the deflection for the forward spectrometer. During data taking we operated these magnets at a field strength of approximately 2 T. The field integral was 5.957 T m, which provides a deflection angle of 60 mrad for ^{28}Si nuclei at the nominal beam momentum of 14.6 GeV/(c nucleon). The reconstruction of beam tracks through the forward spectrometer, in which the known magnetic field and the measured particle trajectories are used to compute an independent value of the beam momentum, yields a mean value of 14.40±0.05 GeV/(c nucleon). The detectors around the target are sensitive to any activity (i.e., neutral or charged particles) in the target region and were used as "veto" detectors to select events that originate from peripheral collisions. Calorimeters provide an energy measurement over the angular interval 2°–165°, and a silicon pad detector measures charged particle multiplicity over the range of 2°–33.5°. The detectors in the forward spectrometer, which consist of tracking detectors, uranium calorimeters, and scintillator hodoscopes, provide momentum, energy and charge measurements for the reaction products passing through the ±12.3 mrad vertical by ±18.4 mrad horizontal aperture centered on the beam axis. To reduce downstream interactions, helium bags were placed in the regions with large gaps between

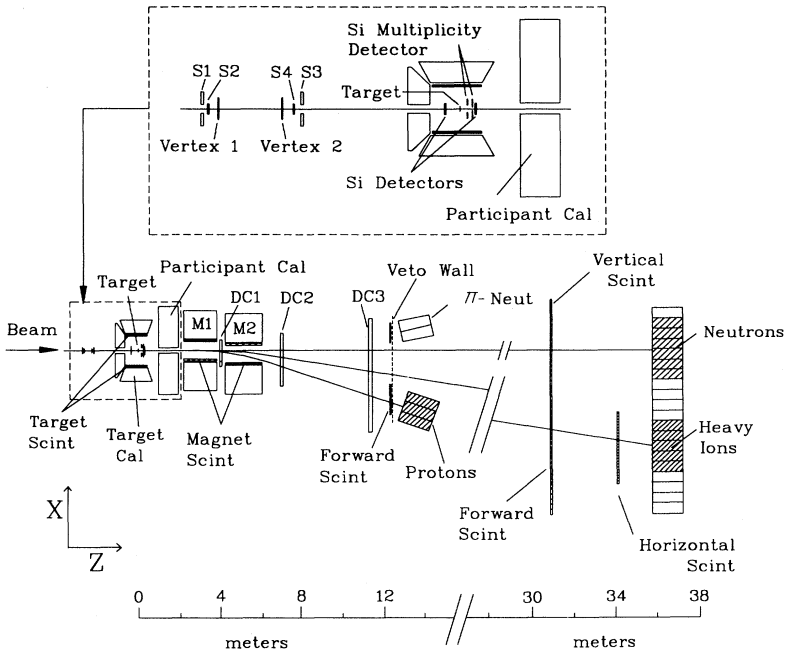

FIG. 1. Diagram of the E814 experimental setup. The beam enters the experiment from the left through a hole in the target calorimeter. Forward-going particles pass through the participant calorimeter opening and the magnets M1 and M2 into the forward spectrometer. Track positions are measured in the three tracking chambers DC1, DC2, and DC3. Charge is measured in the forward scintillator hodoscopes and the energy is measured in the U/Cu/Scint calorimeters.

detectors. In addition, an array of scintillation counters (veto wall) was placed in this region but outside the geometrical acceptance of the spectrometer to detect and veto events in which particles were produced through nuclear interactions. A detailed description of the detectors is given elsewhere [3, 17, 18].

The criteria used for the EMD trigger were based on the selection of events that produce low activity in the detectors around the target. To reduce the background and to enhance the data sample with EMD events, the trigger requires a substantial amount of charge (corresponding to $Z \geq 7$) detected in the scintillators in the region where the heavy fragments are deflected ($Z/A \approx 1/2$). In addition, several triggers were implemented requiring different amounts of energy in the region of the calorimeters that would be struck by protons and neutrons.

The recorded EMD data sample consists of two major parts, namely, single nucleon emission and multinucleon emission. These data were taken with parallel triggers, with each trigger appropriately downscaled to enhance the number of events from decay channels with smaller cross sections in our data sample. Additionally, triggers with and without the veto condition were used. Those with the veto condition produce a sample that is rich in events from EMD.

In addition to the triggers that select events from electromagnetic interactions, several other triggers were used to study trigger efficiency corrections, gain variations, and other systematic effects. These consist of beam triggers, pretriggers (requiring a certain amount of energy in the proton or neutron calorimeters), and random triggers (events with no beam particle present, generated through a random pulser). The frequency of these triggers was adjusted to give a rate of about 5% of the events taken with the EMD triggers. Data were taken with natural targets of Pb, Sn, Cu, and Al, with physical thicknesses of 4.36, 3.35, 2.24, and 1.30 g/cm^2, respectively (corresponding to 4% nuclear interaction lengths for ^{28}Si). In addition, data were taken with an empty target frame to study contributions from interactions in materials other than the target. The total data sample used in this analysis consists of about 2 400 000 EMD and peripheral interaction events.

III. DATA ANALYSIS

A. Event selection

The basic criterion for selecting EMD events is based on the assumption that the electromagnetic processes do not produce significant activity in the target region. In EMD events, the projectile absorbs a virtual photon from the field of the target nucleus and decays by emission of one or more nucleons with rapidity near that of the incident projectile. Nuclear fragmentation, on the other hand, results from hard collisions that in most cases produce particles (e.g., pions) at large angles, which can be detected by the calorimeters in the target region. There are, however, also soft nuclear collisions occurring between the peripheral nucleons from the projectile and the target, that do not produce signals in detectors in the target region. Such events cannot be distinguished from EMD events on an event-by-event basis. It is, however, possible to subtract the nuclear component from the measured cross sections [17], because the nuclear and the electromagnetic cross sections differ in their dependence on the target mass and charge (see Sec. IV A).

The selection criteria were determined by studying the background as well as the target region activity produced by valid beam particles. Valid beam particles were identified by selecting Z=14 particles that entered the ex-

periment through the beam scintillator system and the upstream silicon detector. Requirements were then imposed to select only events where the ^{28}Si projectile does not interact in the target, by measuring the charge and the momentum at the downstream end of the spectrometer. A valid electromagnetic interaction was assumed not to produce more activity than a beam particle that passes through the target without any interaction. The cuts used in this analysis to select EMD events are listed in Table I. A detailed description of these cuts is given elsewhere [17, 18]. We do not observe any target dependence in the overall efficiency of these cuts and hence the same cuts were applied to all targets for the selection of electromagnetic interactions.

The data analysis was carried out by identifying the heavy ion fragment and all the projectile light fragments on an event-by-event basis. Identification of the heavy ion that belongs to specific decay channels reduces the background contributions from other decay channels considerably. This was done by measuring its charge and mass.

The charge of the heavy ion is measured by combining three separate charge measurements. The measurements are done using the silicon detector placed immediately downstream of the target and two scintillator hodoscopes at $z \approx 32$ m, oriented perpendicular to each other (one composed of vertical scintillator plates and the other of horizontal plates). Consistency between the charge measurements ensures that the heavy fragment does not undergo any secondary interaction downstream of the target. Combining the three measurements provides an energy loss resolution of 2.5–3.0 %, adequate to separate different final-state residual ions.

To determine the mass of the heavy fragment we measure the magnetic rigidity P/Z by reconstructing its trajectory through the magnets. We use position measurements given by the tracking chambers DC1, DC2, and DC3 [20–22], combined with the incoming beam angle and position at the target extracted from the beam vertex detector. Our studies show that the residual heavy ion magnetic rigidity can be reconstructed with a resolution of 0.5–1.0 %.

Figure 2 shows the measured charge vs P/Z for heavy ion fragments. The mass of the fragments can be calculated by the relationship $A = (P/Z) \times (Z/P_B)$ where P_B is the beam momentum per nucleon ($\beta \approx 1$ for these fragments). We note a clear separation of the different

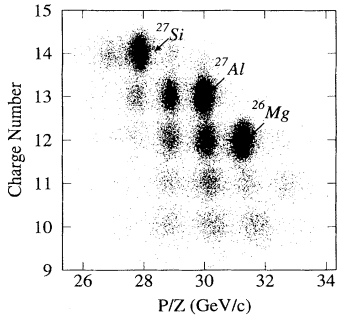

FIG. 2. Measured charge vs the reconstructed magnetic rigidity (P/Z) of the heavy fragments. Each cluster of events corresponds to a single isotope of a given element.

residual heavy fragments. However, the same residual heavy ion can be produced in different decay channels (such as $4p+2n+^{22}$Ne and $2p+1\alpha+^{22}$Ne), and we need therefore additional information from the other detectors to identify specific decay channels.

To identify the decay channels we first select the residual heavy ion through charge and magnetic rigidity measurements. We then inspect the energy in the proton and neutron calorimeters as well as the information from other detectors in the spectrometer. Figure 3(a) shows the measured energy in the neutron calorimeters vs P/Z of the heavy ion, for selected events where the heavy ion is Ne (Z=10). Indicated in the figure are the number of emitted neutrons corresponding to the energy deposited in the neutron calorimeters (along the vertical axis) and the isotope of Ne (along the horizontal axis). We note that for each Ne isotope, the strongest decay channel has two neutrons less than expected for pure nucleon emission. The energy distribution in the proton calorimeters for these channels is compatible with only two protons having been emitted, whereas ΔZ, the difference between the atomic number of ^{28}Si and the atomic number of the residual heavy ion, is 4, indicating an α emission. The magnetic rigidity of the α particles is very close to that of the heavy fragments accompanying them, which limits the efficient track reconstruction for these particles.

The vertical and horizontal hodoscopes at the downstream end of the spectrometer can give additional information to corroborate the presence of the α particle. The α particle was identified by performing a se-

TABLE I. List of cuts used in EMD selection. The events that produce energy and multiplicity less than or equal to the values listed here for each detector were taken as good EMD events.

Detector system	Cut description	Cut
Multiplicity detector	Charge multiplicity	25
Target scintillators	Charge multiplicity	4
Target calorimeter	Energy/cell in side walls	20 MeV
	Energy/cell in back wall	15 MeV
Participant calorimeter	Energy/tower	200 MeV
	Total energy	1 GeV
Magnet scintillators	Charge multiplicity	5
π-neut calorimeters	Energy/tower	0.5 GeV
Neutron region scintillators	Charge multiplicity	3

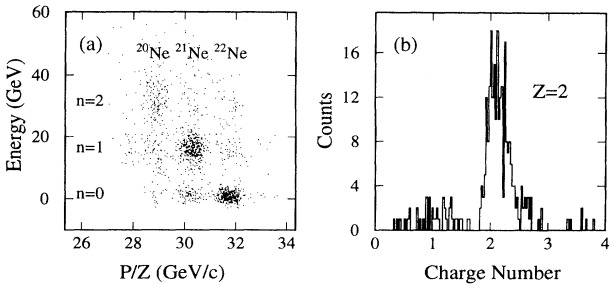

FIG. 3. (a) Measured energy in the neutron calorimeters vs the magnetic rigidity (P/Z) of heavy ion fragments, for selected events where the heavy ion has Z=10. Indicated are the number of neutrons detected in the neutron calorimeters (along the vertical axis) and the isotope of Ne (along the horizontal axis). (b) Measured charge of the particles near the heavy fragments, for $2p1\alpha$ events.

lection on the second highest charge (i.e., the highest charge after identifying the heavy ion) in either the vertical or horizontal scintillation counters. Since the counters are perpendicular to each other, the region where the α particle is not identifiable due to the presence of the heavy ion is limited to an area of about 10×10 cm^2. Figure 3(b) shows the measured charge distribution in the downstream hodoscope for the second highest charge in selected $2p$+1α+^{22}Ne events. The distribution shows a peak corresponding to Z=2 particles, indicating the presence of an α particle. However, the heavy ion sometimes creates δ rays that lead to charge misidentification in the forward scintillators. By examining events in well-identified channels which do not contain an α particle we estimate this background to be 8% in the α sample.

The inefficiencies of the selection procedures are evaluated using data taken from other less restrictive trigger conditions (triggers without the veto condition, pretriggers, and beam triggers). The major contributions to the inefficiency arise from interactions of heavy fragments occurring downstream of the target and the accidental rejection of good events by the trigger. The remaining contributions to the inefficiency come from accidental vetoes in the veto wall, off-line selection for good beam particles, charge identification procedures, cluster algorithms for uranium calorimeters, accidental rejection by off-line vetoes, and heavy fragment track reconstruction. A list of estimated efficiency factors used in this analysis is given in Table II. Some of the efficiency factors are run dependent and were treated accordingly; only the average values are shown in the table. A detailed account of the methods of estimating these efficiency factors is given elsewhere [17, 18].

In addition to the efficiency factors listed in Table II, the spectrometer has limited acceptance for detection of α particles from projectile decay. This inefficiency was estimated using Monte Carlo methods to simulate the decay of specific channels, and evaluating the number of events that fall inside the 10×10 cm^2 area of confusion with the heavy fragment. This estimate depends on the excitation energy, since the opening angle between the heavy ion and the α depends on the energy available for the decay [18]. For the efficiency estimate we have used an average value of 5 MeV above the threshold energy, which yields a value of approximately 70% for the acceptance for all channels involving α emission.

TABLE II. Estimated efficiencies in the identification of the EMD decay channel. These efficiency factors, independent of each other, are evaluated from data taken with less restrictive trigger conditions.

Selection criteria	Efficiency (%)
Downstream interactions	70.6 ± 1.9
On-line veto detectors	76.9 ± 1.4
Veto wall selection	87.5 ± 1.8
Good beam definition	84.3 ± 2.7
Charge identification	93.2 ± 1.5
Single proton clusters	95.8 ± 1.0
Single neutron clusters	90.0 ± 2.0
Off-line veto detectors	96.3 ± 0.5
Track reconstruction	85.2 ± 2.5

Other efficiency factors for complex channels arise from the performance of the calorimeters in detecting multinucleon events (obtained by combining the single nucleon efficiencies given in Table II), and from the $2p$ and $3p$ trigger efficiencies. These amount to 95% and 62%, respectively, and are primarily due to the trigger thresholds imposed on the signals from the calorimeters.

B. Event reconstruction

Reconstructed physical quantities and improved estimates of the track variables were extracted with a reconstruction program that exploits geometrical and kinematical constraints. These constraints allow us to combine the tracking information in an optimal way to determine the parameters of interest.

In the geometrical fit, the angles of the tracks, the coordinates of the vertices, and the momenta of the particles are treated as parameters. Geometrical constraints are imposed when forming the vertices for separate track segments. We constrain all outgoing tracks to have the same (x,y) coordinate at the target and the same x intercept as the incoming beam particle [see Fig. 4(a)]. We are able then to reconstruct $1p$+^{27}Al and $2p$+^{26}Mg channels with three and five geometrical constraints, respectively. The $1n$+^{27}Si system is reconstructed with only one geometrical constraint, since information on the neutrons consists of only the position measurement in the downstream calorimeters (see below).

The kinematics in the data analysis are implemented by performing a kinematically constrained fit. We assume that the decaying ^{28}Si nucleus has the same velocity as the beam particle. The invariant mass is, however, increased by the final-state energy, which is the ^{28}Si excitation energy minus the excitation of the heavy fragment. The final-state energy is introduced as a variable in the fit.

For a two-body decay, two center-of-mass decay angles (θ^* and ϕ^*) are also introduced as variables, along with the horizontal slope and intercept of the incoming track. In this analysis, θ^* is defined as the polar angle of the

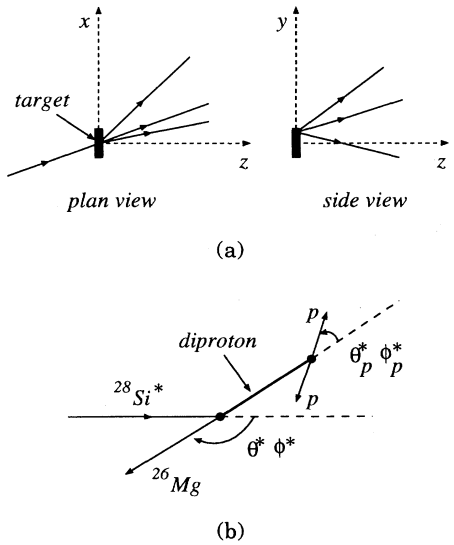

FIG. 4. Diagram illustrating the geometrical and kinematic fits. (a) In the geometrical fit the outgoing tracks and the incoming beam track are required to have a common horizontal (x) intercept. A common vertical (y) intercept is required of the outgoing tracks, but the beam track is not included in the fit, since its vertical coordinates are not measured. (b) The kinematic fit uses as parameters the center-of-mass angles θ^*, ϕ^* (in the projectile rest frame) and θ_p^* and ϕ_p^* (in the diproton rest frame), along with the excitation energy of ^{28}Si, and the invariant mass of the diproton.

momentum vector of the residual heavy ion with respect to the beam momentum vector, in the rest frame of the projectile. This frame is the same as the rest frame of the excited projectile, since the velocity of the projectile is assumed to be unchanged in the EMD process. The azimuthal angle ϕ^* gives the orientation of the decay plane about the beam momentum vector, with $\phi^*=0$ corresponding to the horizontal plane. The masses of the final-state particles are taken from Ref. [23]. The kinematic fit imposes two additional constraints beyond those required by the geometric fit. They are the conservation of the x (horizontal) and z (longitudinal) components of momentum. For the $1p+^{27}$Al seven parameters are needed to describe the collision.

This fitting technique was found to be very useful in reconstructing the $1n+^{27}$Si system, in which the measurement of the neutron momentum is poor, but the position is accurately determined (the calorimetric measurement of the position leads to an accuracy of $\approx$ 2 cm at the downstream end of the spectrometer). If the energy measurement is included in the fit we obtain the same number of constraints for the kinematic fit of the $1n+^{27}$Si system as for the $1p+^{27}$Al system.

The kinematic reconstruction of the three-body decay channel $2p+^{26}$Mg was carried out as a composite two-body decay system [see Fig. 4(b)]. For this purpose ^{28}Si is assumed to decay to a "diproton"$+^{26}$Mg, and the diproton decays into two protons. This is done for convenience in carrying out the kinematic calculations and implies no assumption about the physical decay process since the mass of the intermediate state (diproton) is a free parameter determined from the fit. In the first two-body decay system, the final-state energy (^{28}Si excitation energy minus the excitation energy of ^{26}Mg) is introduced as a variable in the fit. Other variables are the diproton energy (diproton invariant mass minus the mass of the two protons) and the polar and azimuthal angles θ^* and ϕ^* defined above. In the second two-body decay system, two additional angles θ_p^* and ϕ_p^* are introduced. Here θ_p^* is the polar angle of the momentum vector of one of the protons with respect to the diproton momentum vector, in the rest frame of the diproton while ϕ_p^* is the azimuthal angle of the diproton decay plane about the diproton momentum vector, referred to the first decay plane (^{28}Si decay). The number of additional constraints imposed by the kinematics for this channel is also 2.

In this analysis we also introduce parameters to account for the multiple scattering in the horizontal plane. This is done for both proton and heavy ion tracks. Multiple scattering for all material seen by the particles is assumed to be concentrated in the three regions where significant amounts of material are physically located, namely, the target, DC1, and DC2 pad planes. The technique used is the "optimum track fitting method" described by Lutz [24], in which the "observed" value of the scattering angle is zero, and the error in the observation is the calculated rms value of the scattering angle projected onto a plane. Since each parameter is accompanied by an observation, this method introduces no change in the number of degrees of freedom of the fit. We also account for the energy loss resulting from the incoming and outgoing tracks traversing the target.

Approximately 75% of the events from the three selected decay channels were reconstructed successfully. The major loss arises from demanding that there be exactly one hit in each counter of the beam vertex detector. This criterion results in a loss of 15% of the events due to dead or noisy strips in the detector. Of the remaining 10% of the failures, half are lost due to the failure to locate enough hits in either DC2 or DC3 in forming the tracks. The other half of the events are lost in the reconstruction stage, due to the failure of either the geometrical or kinematic fit to converge. These losses are small and are not obviously related to any particular event topology. The distributions of geometrical and kinematic quantities closely resemble those obtained in the simulation (described in the next section). Therefore, we assume that any biases due to reconstruction inefficiencies are negligible.

IV. RESULTS

A. Cross sections

Cross sections were evaluated for every identified ^{28}Si decay channel for Pb, Sn, Cu, and Al targets. The results are shown in Table III. The listed errors are only statistical. The overall cross-section scale is uncertain by 6.5% due to the systematic errors in the measurements. These data are corrected for the detection efficiencies discussed previously and for interactions outside the target, by sub-

tracting the appropriately scaled rates of events observed with the empty target frame. Correction for the multiple interaction background (discussed below) are not made, but channels in which our estimate of this background exceeds 5% (for the Pb target) are indicated. The empty target contributions for Pb, Sn, Cu, and Al targets are 5%, 8%, 15%, and 32%, respectively. Figure 5 shows the measured cross sections as a function of the target atomic number Z_T. The dependence of the cross section on the target charge behaves approximately as $Z_T^{1.8}$ for high Z targets (dashed lines in Fig. 5), as expected for EMD at AGS energies [25]. The data for the low Z targets show a deviation from this simple $Z_T^{1.8}$ dependence. The multinucleon emission channels show a larger deviation than simple channels.

In Fig. 6 we show our measured cross sections (open circles) and calculated cross sections for a few dominant decay channels for the Pb target. The cross sections are calculated by taking the product of the Weizsäcker-Williams (WW) virtual photon spectrum and the measured photonuclear cross sections for the $\sigma(\gamma,p)$, $\sigma(\gamma,n)+\sigma(\gamma,np)$, and $\sigma(\gamma,\alpha)$ taken from the literature [4–6]. There is excellent agreement between our data and the calculation. Due to the lack of precise measurements of $\sigma(\gamma,2p)$ cross sections we were unable to calculate the cross section for the $2p+^{26}$Mg decay channel.

It is also possible to compare the measured cross sections with those obtained from calculations based on the statistical model [26, 27], which is the application of the Hauser-Feshbach formalism for the description of the decay of excited nuclei. The flux and energy spectrum of the (equivalent) photons seen by the projectile is assumed to be described by the WW equations and the total absorption cross sections are taken to be those measured using real photons [28–31]. The absorption brings the nucleus to an excitation energy equaling that of the incident photon, and the subsequent decay proceeds with the branching ratios given by the code CASCIP [27]. This code includes a detailed treatment of the nuclear isospin. The calculated decay probabilities for specific final states are significantly influenced by the degree to which isospin is a conserved quantity during the reaction.

The $1p+^{27}$Al channel measured with good statistics and low systematic errors in these data are, according to the calculations, quite sensitive to the degree of isospin mixing in the excited projectile. The calculated Pb target cross sections change from 875 mb to 650 mb as the assumed isospin is varied from the pure isospin of the doorway GDR to the complete isospin mixing of the compound nucleus. The experimentally measured strength of 676±45 mb for this target implies substantial, if not complete, isospin mixing for this channel, in disagreement with that deduced from the studies with real photons [28, 31] which favor isospin conserving direct decays. The $\alpha+^{24}$Mg final state is another channel populated by a single photon from the GDR that is sensitive to the degree of isospin mixing. The calculated Pb target cross section for this channel is 13 mb for isospin conservation and 300 mb for complete isospin mixing. The measured cross section of 72±32 mb indicates a nearly perfect conservation of the isospin, in agreement with measurements of cross sections performed with real photons. The origin of this discrepancy is not understood. It might reflect different combinations from direct and statistical decays to the two reaction channels considered here.

Our total EMD cross section measured by the interaction of ^{28}Si in a Pb target is 1310±90 mb. This value, which sets an upper bound on the sum of our exclusive cross sections is obtained by using an unbiased (beam trigger) event sample. If we add the exclusive cross sections given in Table III we obtain 1210±85 mb (including statistical and systematic errors), indicating that our exclusive cross-section measurements account for the measured total EMD cross section. From the WW calculation

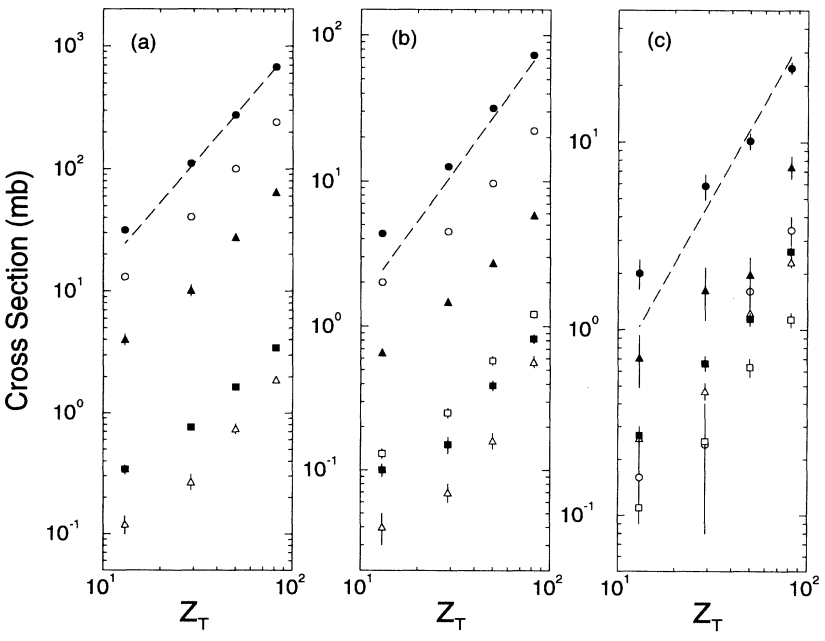

FIG. 5. Measured peripheral cross sections as a function of the target atomic number Z_T for a few decay channels. They are (a) $1p+^{27}$Al (solid circles), $1n+^{27}$Si (open circles), $1p1n+^{26}$Al (solid triangles), $2n+^{26}$Si (open triangles), and $1p2n+^{25}$Al (solid squares); (b) $2p+^{26}$Mg (solid circles), $2p1n+^{25}$Mg (open circles), $2p2n+^{24}$Mg (solid triangles), $3p+^{25}$Na (open triangles), $3p1n+^{24}$Na (solid squares), and $3p2n+^{23}$Na (open squares); (c) $1p1\alpha+^{23}$Na (solid circles), $1n1\alpha+^{23}$Mg (open circles), $1p1n1\alpha+^{22}$Na (solid triangles), $2p1\alpha+^{22}$Ne (open triangles), $2p1n1\alpha+^{21}$Ne (solid squares), $2p2n1\alpha+^{20}$Ne (open squares). The dashed lines indicate the expected $Z_T^{1.8}$ dependence of the cross sections.

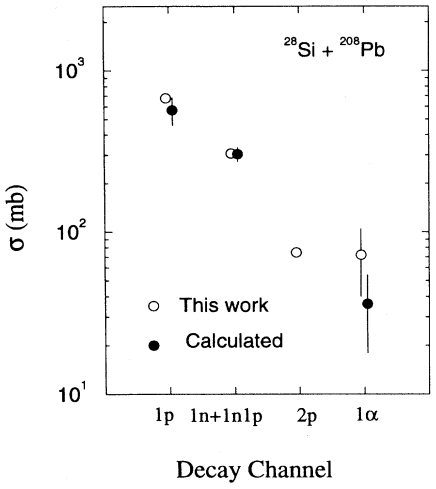

FIG. 6. Measured EMD cross sections (open circles) compared with the calculated cross sections (solid circles) in the WW framework.

we expect the total integrated EMD cross section to be roughly 1600±100 mb (using the measured $\sigma(\gamma,\text{tot})$ total photon absorption cross sections for 0–30 MeV from [31] and for 30–100 MeV from [32]) which is significantly higher than our measurements. However, while previous measurements of the total photon absorption cross section [33, 34] show approximately the same shape, they differ by as much as 20% in the overall cross section scale from those of [31], in closer agreement with our data.

The fragmentation of ^{28}Si at 14.6 GeV/(c nucleon) has been measured by Brechtmann *et al.* [32] using plastic nuclear track detectors. Their measurements report a total charge changing ($\Delta Z \geq 1$) EMD cross-section value of 1190±170 mb for the Pb target. This is consistent with our results if we subtract the $1n$ and $2n$ contributions (243 mb) from our total EMD cross section. The EMD cross sections for the Pb target obtained from our measurements as a function of ΔZ are displayed in Fig. 7 (open circles), along with the results of Brechtmann *et al.* (solid circles). The agreement is excellent. One should note that in the present work we select events from EMD on an event-by-event basis whereas in [32] the total (EMD + nuclear) cross sections are measured and the EMD and nuclear components are separated using factorization.

One of the physical processes expected to occur in EMD is multiphoton excitation, where the projectile absorbs two or more virtual photons from the same target nucleus. In the harmonic approximation of nuclear excitation, the N photon absorption should appear at roughly $N \times E_{\text{GDR}}$ and should have a width of approximately $\frac{3}{2}N \times \Gamma_{\text{GDR}}$ where Γ_{GDR} is the width for sin-

TABLE III. Measured exclusive EMD cross sections for channels having protons, neutrons, and α particles in the final state. The listed errors are only statistical. The overall cross-section scale is uncertain by 6.5% due to the systematic errors in the measurements. Values shown here do not contain corrections for the multiple interaction background as discussed in the text, due to our lack of knowledge of the relevant cross sections. We have made rough estimates of this background in order to understand its effect on the Z_T dependence of the cross sections. Channels where the estimated background exceeds 5% of the measured cross sections for the Pb target are shown in parentheses.

Decay channel	-Q (MeV)	Pb (mb)	Sn (mb)	Cu (mb)	Al (mb)
^{27}Al+1p	11.6	676.4±7.6	274.0±4.4	111.0±3.3	31.6±1.2
^{27}Si+1n	17.1	241.0±4.2	100.0±2.0	40.4±1.7	13.11±0.59
^{26}Al+1p1n	24.7	65.1±2.5	27.5±1.4	10.2±1.1	4.04±0.43
^{26}Mg+2p	19.8	73.11±0.80	31.70±0.41	12.55±0.16	4.35±0.10
^{25}Mg+2p1n	30.9	22.28±0.44	9.66±0.26	4.49±0.15	2.00±0.08
^{24}Mg+2p2n	38.3	5.82±0.23	2.72±0.14	1.47±0.08	0.66±0.04
(^{26}Si+2n)	30.5	1.90±0.11	0.74±0.07	0.27±0.04	0.12±0.02
^{25}Al+2n1p	36.0	3.45±0.15	1.64±0.09	0.76±0.05	0.34±0.03
(^{25}Na+3p)	34.0	0.57±0.05	0.16±0.02	0.07±0.01	0.04±0.01
(^{24}Na+3p1n)	43.0	0.82±0.06	0.39±0.03	0.15±0.02	0.10±0.01
^{23}Na+3p2n	49.9	1.21±0.07	0.58±0.04	0.25±0.02	0.13±0.01
(^{24}Ne+4p)	44.7	0.011±0.006	0.002±0.002	–	–
(^{23}Ne+4p1n)	53.6	0.016±0.008	0.006±0.005	0.004±0.003	0.003±0.002
(^{22}Ne+4p2n)	58.8	0.109±0.018	0.053±0.011	0.025±0.006	0.015±0.004
^{21}Ne+4p3n	69.1	0.073±0.015	0.050±0.011	0.037±0.008	0.007±0.003
^{24}Mg+1α	10.0	72±32	58±30	17±19	21±16
^{23}Na+1p1α	21.7	24.7±1.7	10.2±1.0	5.83±0.90	2.00±0.36
^{23}Mg+1n1α	26.5	3.41±0.60	1.60±0.30	0.24±0.16	0.16±0.07
^{22}Na+1p1n1α	34.1	7.4±1.0	1.97±0.46	1.63±0.51	0.71±0.22
^{22}Ne+2p1α	30.5	2.30±0.15	1.23±0.09	0.47±0.05	0.26±0.03
^{21}Ne+2p1n1α	40.8	2.61±0.15	1.14±0.09	0.66±0.06	0.27±0.03
^{20}Ne+2p2n1α	47.6	1.13±0.10	0.63±0.07	0.25±0.03	0.11±0.02

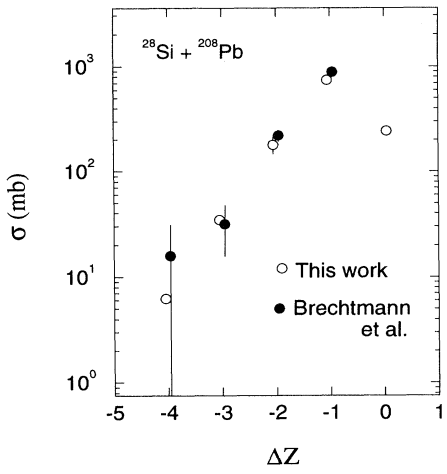

FIG. 7. Semi-inclusive EMD cross sections for Pb target measured in this experiment (open circles) compared to inclusive charge-changing ($\Delta Z = Z_{\rm frag} - Z_{\rm proj}$) EMD cross sections measured with emulsions (solid circles) [32].

gle photon absorption [14]. For our beam energy and for Si projectiles interacting on a Pb target, the expected energy-integrated ratio of two-photon absorption to single photon absorption is roughly 5% in the region $E_{\rm GDR} \geq 30$ MeV (we expect the two-photon excitation to peak near 40 MeV since the single photon absorption occurs approximately at 20 MeV), which indicates the required sensitivity to observe DGDR in our experimental situation. The simplest approach to look for signatures from the DGDR excitation in energy-integrated cross sections is to look for deviations from the $Z_T^{1.8}$ behavior [14]. If two photons are absorbed by the projectile, the cross section should display a target dependence close to Z_T^4. If the one-photon processes are competing with the two-photon processes, the dependence would be intermediate between $Z_T^{1.8}$ and Z_T^4.

To test the existence of multiphoton excitations we extract the Z_T dependence (exponent) of the EMD cross sections for all the available decay channels, using the following parametrization for the cross sections:

$$\sigma = a \times (A_T^\alpha + A_P^\alpha - \delta) + b \times Z_T^c \qquad (1)$$

with α=1/3, δ=0, and a, b, and c free parameters. The exponent of Z_T was extracted by fitting the parameters in the formula using cross sections for Pb, Sn, Cu, and Al targets. To test the sensitivity of our results to the assumed form of the nuclear term in the above equation we have varied the quantities α and δ. For values of α between $\frac{1}{4}$ and $\frac{2}{3}$ and values of δ between 0 and 2, the variation of c is within its statistical errors.

One possible background to the two-photon process could originate from the absorption of two single photons from different target nuclei, which could contribute to an increase in the exponent. We estimate this background using the assumption that the nucleon removal cross sections are the same whether it is the first or the second interaction in the target material. That is, after the first interaction the residual nucleus will behave in subsequent interactions as the original projectile. The measured cross sections are corrected for this multiple interaction background and refit in order to obtain the corrected values for the exponents. The exponents extracted for several decay channels with the smallest statistical and systematic errors are shown in Fig. 8 as a function of the Q value for the reaction. Within errors it is seen that all values of the exponent are consistent with a value of 1.8, as expected for single photon excitation.

A comparison of the exponents for the $1p$ and $2p$ emission processes can be used to set an upper limit on the DGDR amplitude. Because the $1p$ excitation energy distribution is dominated by the GDR, which is suppressed in the $2p$ channel due to its higher threshold, the presence of DGDR should result in a larger value of c for the $2p$ channel. For the $2p$+^{26}Mg channel we find c = 1.80±0.03, while for the $1p$+^{27}Al channel we find c = 1.85±0.04, yielding Δc = −0.05±0.05, consistent with zero. To understand the relationship between the values of the exponent c and the DGDR amplitude we have used the fit to Eq. (1), increasing all of our cross sections by a term proportional to Z_T^4 and refitting for the value of c. For a DGDR contribution which increases the Pb target cross section by 10% we find that the exponent increases by Δc = 0.14, which would have been detectable at the 3σ level in this experiment. Thus, we conclude that our data exclude at the 95% confidence level, a DGDR contribution to the $2p$ channel of 10% for the Pb target, consistent with the theoretical predictions [14]. Recent data for EMD of ^{136}Xe show DGDR amplitude at a level of approximately twice the expected values [9]. At AGS energies the virtual photon spectrum drops less rapidly with the photon energy than at lower beam energies, such that at $E_\gamma \approx 40$ MeV, where the double photon processes are expected to be seen, the single photon processes are expected to dominate [15]. Also the GDR in the relatively light nucleus ^{28}Si is considerably fragmented and its width is larger than that of ^{130}Xe, which may lead to an even wider, harder to detect DGDR. We note that a small nonzero value of Δc was observed for decay channels with $Q > 25$ MeV listed in

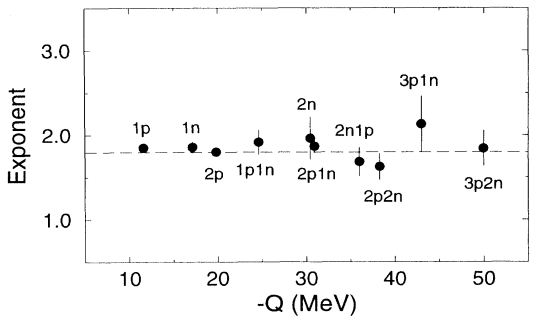

FIG. 8. Values of the exponent of Z_T in Eq. (1) found from fitting the data given in Table III for the decay channels with the smallest statistical and systematic errors (after correcting for the double interaction background as discussed in the text), as a function of the Q value of the reaction. The decay channel $3p$+^{25}Na is eliminated from this plot for reasons discussed in the text.

Table III from an independent analysis performed on the same data set [35]. Given the systematic errors for those channels arising mainly from the two-step background, the two analyses are consistent.

B. Final-state energy

Excitation energy distributions measured in relativistic collisions between heavy ions can produce valuable information for the understanding of nuclear structure and for searching for structures excited by higher order processes. For this purpose we reconstruct the final-state energy distributions for the $1p$+^{27}Al, $1n$+^{27}Si, and $2p$+^{26}Mg decay channels of ^{28}Si, excited through electromagnetic interactions. The results for the $1p$+^{27}Al reconstruction were reported previously [17, 19].

The reliability of the programs used in the reconstruction was tested by using simulated events. The positions of the tracks for known kinematic conditions were simulated in all of the detection planes of the experimental apparatus. The uncertainties of the position measurements and the effects that arise from multiple scattering are included in the simulation to smear the track locations at each detection plane. We simulated multiple scattering in the air and in other materials in the path of the tracks, including the target and the material in the various detectors. In addition, the response of the neutron calorimeter energy distribution was included in the simulation, to study the $1n$+^{27}Si channel. For this channel the energy measurements of the neutron calorimeters play an essential role. In the study of the $2p$+^{26}Mg channel, the simulation was used extensively to develop specific pattern recognition methods for the proton tracks, where an additional complication arises due to the very small opening angle between the tracks. This occurs because the protons are emitted with a very low kinetic energy in the rest frame of the projectile.

The simulation also allows a study of various factors that affect the resolution of the reconstructed quantities. These arise mainly from the detector resolution and by multiple scattering (for example, in the air) not accounted for by the optimum track fitting method. We estimate an energy resolution of the reconstructed final-state energy of 1 MeV for the $1p$+^{27}Al and 2 MeV for the $1n$+^{27}Si and $2p$+^{26}Mg channels in the data taken with a Pb target. An estimate of the systematic errors in the final-state energy scale is also obtained from the simulation code. They arise from uncertainties in the beam momentum, the field strength, the effective magnetic length of the spectrometer magnets, and the detector alignment constants. The estimated systematic error is less than 0.5 MeV.

Figure 9 shows the reconstructed final-state energy distributions for the $1n$+^{27}Si and $2p$+^{26}Mg decay channels obtained for four different targets. The normalization for these data was chosen so that the integral of each of the distributions yields the cross sections shown in Table III, thereby correcting for the reconstruction inefficiencies discussed in Sec. III B. The arrows in the figure indicate the kinematic thresholds of the reactions. In the $1n$ data, the tail out to high energies ($>$ 40 MeV)

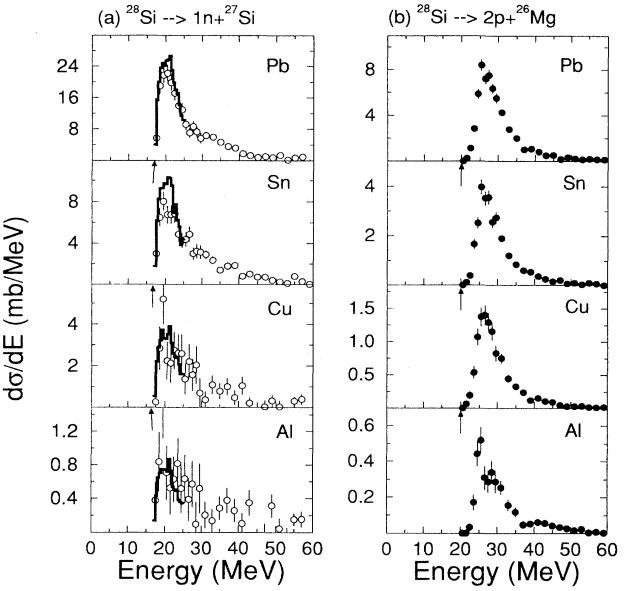

FIG. 9. Reconstructed final-state energy distributions for Pb, Sn, Cu, and Al targets. The arrows indicate the kinematic thresholds of the decay. (a) $1n$+^{27}Si. The solid curves are obtained from $\sigma(\gamma,n)$ experimental data multiplied by the virtual photon spectrum and simulated through our apparatus. See [17] for similar comparisons with $\sigma(\gamma,p)$ data. (b) $2p$+^{26}Mg.

is a result of our limited resolution in the measurement of the neutron energy. The distributions shown are corrected for interactions outside of the target by subtracting the appropriately scaled distribution obtained with the empty target frame. As with the integrated cross-section measurements, the distributions for the heavier targets should not be significantly contaminated by peripheral nuclear interaction events. The nuclear contamination can reach 40–50 % for the Al target and the background level can vary over the excitation spectrum [17]. In Figs. 10(a), 10(b), and 10(c) we show, on the same scale, the reconstructed final-state energy distributions for $1p$, $1n$, and $2p$ emission channels induced by the Pb target. The distributions clearly show that these three decay channels are strongly influenced by excitation of the GDR in ^{28}Si. Due to the reaction thresholds, only the higher energy part of the resonance is seen for the $1n$ and $2p$ channels.

To compare our measured final-state energy distributions with the available data on ^{28}Si photonuclear reactions [4–6] we have incorporated an event generator in our simulation code. It produces events having an excitation energy distribution given by the product of the photonuclear cross sections and the virtual photon spectrum. These events are then reconstructed with the same code used for real events. The results so obtained for the $1n$+^{27}Si channel are shown in Fig. 9 (solid curve). A meaningful comparison can only be made for excitation energy $<$ 24.6 MeV, since above 24.6 MeV the available data on (γ,n) include contributions from (γ,pn) channel. The experimental and the calculated distributions

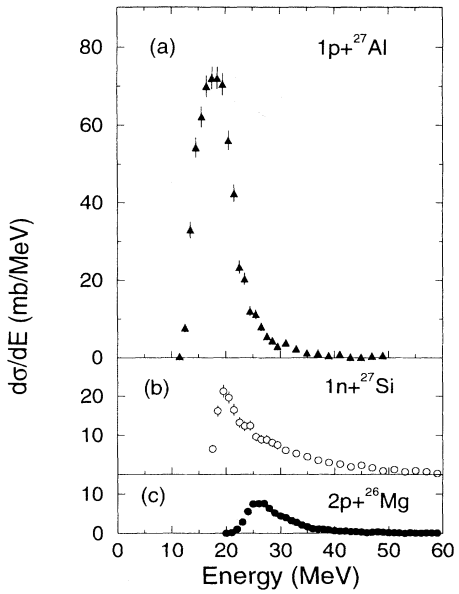

FIG. 10. Reconstructed final-state energy distributions for (a) $1p$+^{27}Al, (b) $1n$+^{27}Si, and (c) $2p$+^{26}Mg decay channels for the Pb target.

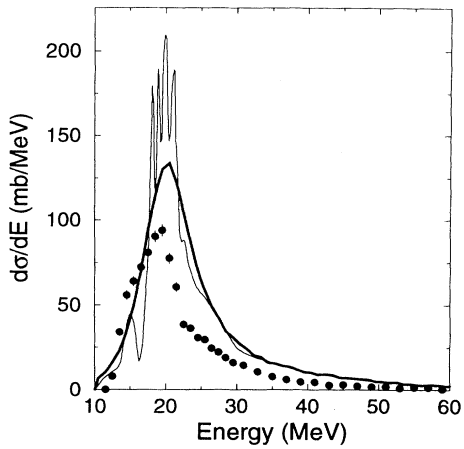

FIG. 11. Sum of the cross sections for the three reconstructed decay channels (solid circles) compared to the measured total photon absorption cross section of ^{28}Si. The thin curve corresponds to the total photon absorption spectrum multiplied by the WW virtual photon spectrum, and the thick curve is the thin curve folded with a Gaussian of σ=2 MeV to simulate the effect of the experimental resolution. As discussed in the text, values of the absolute cross section for $\sigma(\gamma,\text{tot})$ 20% lower than those used here have also been reported.

agree well in this region. For the Pb target we measure in the energy region from 17.0–24.5 MeV an integrated cross section value of 132 ± 12 mb whereas the calculation gives 152 ± 20 mb. The excess of the measured cross sections compared to the calculations, especially for light targets, is probably due to the nuclear component in the measured cross sections. From the fitting procedure discussed in Sec. IV A we estimate that the nuclear contamination in the measured cross sections changes from 3% to 40% between the Pb and Al targets, in agreement with the trend observed in Fig. 9.

The cross sections measured for $1p$, $1n$, and $2p$ emission channels induced by the Pb target sum to about 1000 mb, which represents roughly 80% of the measured total EMD cross section. This permits a comparison between the sum of our reconstructed final-state energy distributions with the measurements of total photon absorption cross sections [31, 32]. This is shown in Fig. 11 where the thin curve corresponds to the total photon absorption spectrum multiplied by the WW virtual photon spectrum and the thick curve is the thin curve convoluted with a Gaussian of σ=2 MeV. Although we measure only 80% of the total cross section in these three channels (solid circles) they reproduce the shape of the total EMD cross section quite well. As mentioned above, values of the total photon absorption cross section similar in shape but 20% lower than the data used here have also been reported. We emphasize here that the distributions from the photonuclear reactions are of excitation energies in ^{28}Si, but our reconstructed distributions are of "final-state energy"—the excitation energy of ^{28}Si minus the excitation energy of the residual heavy ion after the decay. For the $1p$ emission channel [3], it was shown that the final-state energy distribution is broadened and "stretched" toward the low energy side compared to the excitation energy spectrum, which is qualitatively observed in Fig. 11.

In Fig. 12 we show the angular distributions from the $2p$ emission channel induced by the Pb target. Here θ^* and ϕ^* are the polar and azimuthal angles of ^{26}Mg in the projectile frame and θ_p^* and ϕ_p^* are the angles of the protons in the diproton frame. Within statistics they show a nearly flat distribution for $\cos\theta^*$ and for ϕ^*, indicating an approximately isotropic emission. In particular, as was already noted for the $1p$ emission channel [3], no preference is seen for emission perpendicular to the beam axis, as suggested by Bertulani and Baur [13]. In Fig. 12(a) we show for comparison the dependence predicted by their calculation for spinless projectiles and fragments (solid line). For the $1n$ emission channel we were unable to extract the center-of-mass angular distributions due to limited energy and position resolution (for track reconstruction) in the calorimeters.

To complete this discussion we show in Fig. 13(a) the kinetic energy distribution of one of the protons in the rest frame of the projectile from the $2p$+^{26}Mg decay channel. For comparison we show in Figs. 13(b) and 13(c) the kinetic energy of the protons from the $1p$+^{27}Al decay channel and the neutrons from the $1n$+^{27}Si decay channel, respectively. We see that both the distributions for the protons in $2p$+^{26}Mg and for the neutrons in $1n$+^{27}Si are peaked at very low values of kinetic energy. This reflects the fact that these channels mainly come from the GDR of ^{28}Si (see Fig. 10), and in view of the reaction thresholds, very little energy is left for the emitted particles. The low kinetic energy of the protons in the $2p$ channel causes them to be emitted with a very small opening angle, demanding special reconstruction

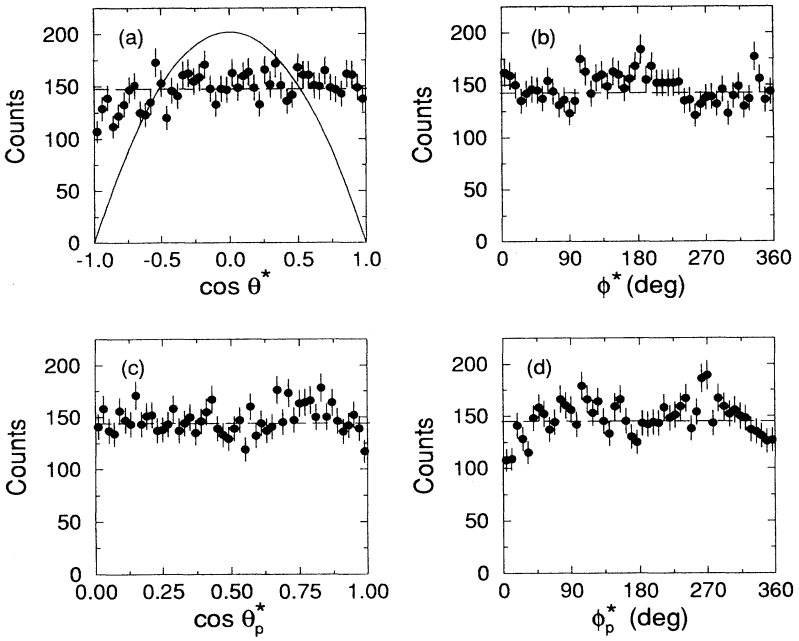

FIG. 12. Angular distributions for the $2p$+^{26}Mg channel. (a) Polar angle of the ^{26}Mg momentum vector with respect to the beam momentum vector, in the rest frame of the ^{28}Si projectile. (b) Azimuthal angle of the decay plane about the beam momentum vector in the first two-body decay system, ^{28}Si $\rightarrow$ "diproton"+^{26}Mg (see text). (c) Polar angle of the momentum vector of the protons with respect to the momentum vector of the diproton, in the rest frame of the diproton (see text). (d) Azimuthal angle of the proton decay plane about the diproton momentum vector. The solid line represents the predicted dependence for spinless projectiles and fragments [13] and the dashed lines are drawn at the mean values of the distributions.

techniques (see Sec. III B).

Excitation of the DGDR is expected to produce an enhancement in the measured excitation energy spectrum since the DGDR contribution increase as $\sim Z_T^4$. No such enhancement is visible in our spectra. From the measurements of the integrated EMD cross sections we set an upper limit of 10% (for the Pb target) on the fraction of the cross section due to the two-photon process in the $2p$ channel. We do not set a similar limit from the shape of the excitation energy distribution since a Gaussian of this amplitude with the expected parameters (centered at 40 MeV with a width of about 20 MeV) would not stand out from the tail of the spectrum due to single photon excitation. We conclude that the sensitivity of DGDR in the excitation energy distribution is inferior to that found from the Z_T dependence.

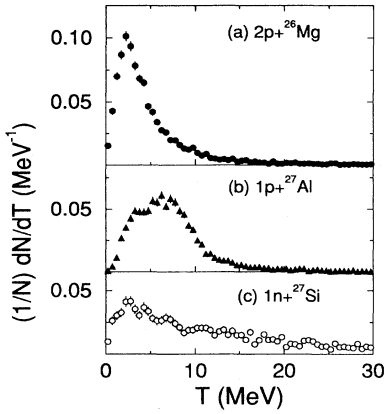

FIG. 13. Kinetic energy (T) of the protons emitted in (a) $2p$+^{26}Mg and (b) $1p$+^{27}Al, and neutrons emitted in (c) $1n$+^{27}Si, in the rest frame of the projectile.

By taking the ratios of the excitation spectra for different targets we can obtain the Z_T dependence of partial cross sections as a function of energy. This is a different way to search for the two-photon excitation. In Figs. 14(a) and 14(b) we show the ratios for Pb/Sn and Pb/Al (solid circles). We have added the $1p$+^{27}Al and $2p$+^{26}Mg decay channels to increase the statistics (due to limited resolution in the reconstruction, the $1n$+^{27}Si decay channel was not used here). The short-dashed lines in the figure correspond to the calculated ratios of the WW photon spectrum and thus correspond to the ratio

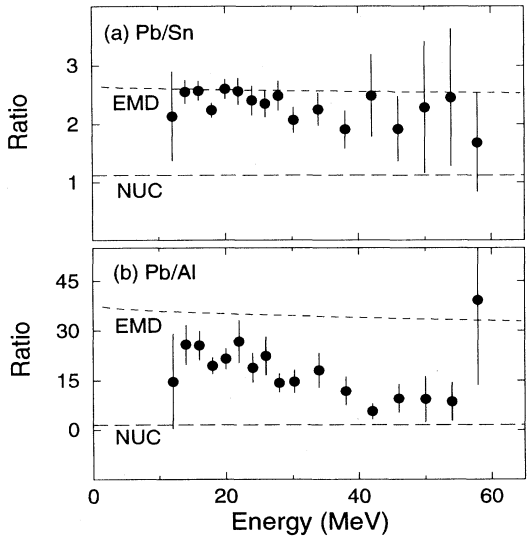

FIG. 14. Ratio of excitation energy spectra. The long-dashed lines represent the expected ratio for pure nuclear behavior. The short-dashed lines represent the ratio obtained with WW photon spectra for pure single photon EMD behavior. (a) Pb/Sn. (b) Pb/Al.

expected for pure single photon excitation. The long-dashed lines correspond to the ratio for pure nuclear contributions [$b = 0$ in Eq. (1)]. The data indicate a substantial increase in the nuclear contribution for the Al target. No enhancement around 40 MeV is evident. Rather, the ratios for Pb/Sn, where the nuclear background is small, show a behavior in close agreement with single photon absorption.

V. CONCLUSIONS

We have presented new results on exclusive cross-section measurements for a large number of decay channels from the electromagnetic dissociation of 14.6 GeV/(c nucleon) ^{28}Si. Our enriched sample of EMD events permits extraction of cross sections down to the microbarn level. The sum of our exclusive cross-section values agrees with our measurement of the total EMD cross section obtained from untriggered events and with the inclusive results from emulsion experiments.

The dependence of the cross sections on the target atomic number Z_T is consistent with the expected value of $Z_T^{1.8}$. No enhancement of the exponent was observed for channels with Q values around 40 MeV as expected for two-photon excitation. From our data we can set an upper limit of 10% for the DGDR contribution to the Pb target cross section for the $2p$+^{26}Mg decay channel.

We have reconstructed the final-state energy distributions for the $1n$+^{27}Si and $2p$+^{26}Mg emission channels with a resolution of the order of 2 MeV. These data complement similar data obtained previously on the $1p$+^{27}Al channel. The $1n$ data are well described by the product of the experimental cross section $\sigma(\gamma,n)$ with the calculated virtual photon spectrum. A similar comparison for the $2p$ channel cannot be made, due to the lack of precise experimental data for the cross section $\sigma(\gamma,2p)$. For this channel the measured proton angular distributions are consistent with isotropic emission. The sum of the cross sections for the $1p$, $1n$, and $2p$ channels account for close to 80% of the total EMD cross section. The corresponding energy distribution is in good agreement with the measured $\sigma(\gamma,\text{tot})$ cross section multiplied by the WW virtual photon spectrum. These data clearly demonstrate that the EMD proceeds mainly by the excitation of the GDR in ^{28}Si. Our experiment shows that it is possible at these very high energies to reconstruct the excitation energy of excited projectiles with a sufficiently good energy resolution to study the structure of the inelastically scattered nuclei.

ACKNOWLEDGMENTS

We acknowledge the excellent support by the BNL AGS and Tandem staffs and Dr. H. Brown for expert help in the design and running of our beam line. This research is supported, in part, by the U.S. Department of Energy, the National Science Foundation, the Natural Sciences and Engineering Research Council of Canada, and the Conselho Nacional de Pesquisa e Desenvolvimento (CNPq).

[1] J.D. Jackson, *Classical Electrodynamics* (Wiley, New York, 1975), p. 719, and references given therein.
[2] P. Braun-Munzinger *et al.*, Proposal 814 submitted to the AGS Program Committee, accepted 1985.
[3] E814 Collaboration, J. Barrette *et al.*, Phys. Rev. C **41**, 1512 (1990).
[4] R.L. Gulbranson, L.S. Cardman, A. Doron, A. Erell, K.R. Lindgren, and A.I. Yavin, Phys. Rev. C **27**, 470 (1983).
[5] E. Kerkhove, P. Berkvens, R. Van de Vyer, H. Ferdinande, P. Van Otten, D. Ryckbosch, and E. Van Camp, Nucl. Phys. **A474**, 397 (1987).
[6] R.E. Pywell, B.L. Berman, J.W. Jury, J.G. Woodworth, K.G. McNeil, and M.N. Thompson, Phys. Rev. C **27**, 960 (1983).
[7] S. Mordechai *et al.*, Phys. Rev. Lett. **61**, 531 (1988).
[8] J. Ritman *et al.*, Phys. Rev. Lett. **70**, 533 (1993).
[9] R. Schmidt *et al.*, Phys. Rev. Lett. **70**, 1767 (1993).
[10] T. Aumann, J.V. Kratz, E. Stiel, K. Sümmerer, W. Brüchle, M. Schädel, G. Wirth, M. Fauerbach, and J.C. Hill, Phys. Rev. C **47**, 1728 (1993).
[11] G. Baur and C.A. Bertulani, Phys. Lett. B **174**, 23 (1986); Phys. Rev. C **34**, 1654 (1986).
[12] G. Baur and C.A. Bertulani, Nucl. Phys. **A482**, 313c (1988).
[13] C.A. Bertulani and G. Baur, Phys. Rep. **163**, 299 (1988), and references given therein.
[14] W.J. Llope and P. Braun-Munzinger, Phys. Rev. C **41**, 2644 (1990).
[15] W.J. Llope and P. Braun-Munzinger, Phys. Rev. C **45**, 799 (1992).
[16] V.Yu. Ponomarev, E. Vigezzi, P.F. Bortignon, R.A. Broglia, G. Colo, G. Lazzari, V.V. Voronov, and G. Baur, Phys. Rev. Lett. **72**, 1168 (1994).
[17] E814 Collaboration, J. Barrette *et al.*, Phys. Rev. C **45**, 2427 (1992).
[18] U. Sonnadara, Ph.D. Dissertation, University of Pittsburgh (1992).
[19] U. Sonnadara for the E814 Collaboration, in *Proceedings of the Gull Lake Nuclear Physics Conference on Giant Resonances* [Nucl. Phys. A **569**, 149c (1994)].
[20] B. Yu, Ph.D. Dissertation, University of Pittsburgh (1991).
[21] R. Debbe *et al.*, IEEE Trans. Nucl. Sci. **37**, 88 (1990).
[22] J. Fischer *et al.*, IEEE Trans. Nucl. Sci. **37**, 82 (1990).
[23] A.H. Wapstra and K. Bos, At. Data Nucl. Data Tables **19**, 177 (1977).
[24] G. Lutz, Nucl. Instrum. Methods Phys. Res. Sect. A **273**, 349 (1988).
[25] D. Lissauer and H. Takai, Phys. Rev. C **41**, 2410 (1990).
[26] CASCADE, F. Pühlhofer, Nucl. Phys. **A280**, 267 (1977).
[27] CASCIP, an extended version of the code CASCADE, M.N. Harakeh (private communications).
[28] J. Ahrens, Nucl. Phys. **A446**, 229c (1985).
[29] J.E.M. Thomson and M.N. Thomson, Nucl. Phys. **A285**, 84 (1977).
[30] R. Alarcon, A.M. Nathan, S.F. LeBrun, and S.D. Hoblit, Phys. Rev. C **39**, 324 (1989).
[31] J. Ahrens, H. Borchert, K.H. Czock, H.B. Eppler, H. Gimm, H. Gundrum, M. Kröning, P. Riehn, G. Sita Ram,

A. Zieger, and B. Ziegler, Nucl. Phys. **A251**, 479 (1975).
[32] C. Brechtmann, W. Heinrich, and E.V. Benton, Phys. Rev. C **39**, 2222 (1989).
[33] N. Bezić, D. Jamnik, G. Kernel, J. Krajnik, and J. Snajder, Nucl. Phys. **A117**, 124 (1968).
[34] J.M. Wyckoff, B. Ziegler, H.W. Koch, and R. Uhlig, Phys. Rev. B **576**, 137 (1965).
[35] W.J. Llope, Ph.D. Dissertation, SUNY at Stony Brook (1992); W.J. Llope for the E814 Collaboration, in "Proceedings of the Notre Dame Workshop on Giant Resonances and Related Phenomena," edited by U. Garg, Notre Dame, 1992 (unpublished).